Hydrodynamic analysis of a novel multi-buoy wind-wave energy system

Yanni Li[a], Shiqiang Yan[b], Hongda Shi[a,c,d], Qingwei Ma[b], Demin Li[a], Feifei Cao[a,c*]

[a] College of Engineering, Ocean University of China, 238, Songling Road, Qingdao, 266100, China

[b] School of Science & Technology, City, University of London, London, EC1V 0HB, United Kingdom

[c] Shandong Provincial Key Laboratory of Ocean Engineering, 238, Songling Road, Qingdao, 266100, China

[d] Pilot National Laboratory for Marine Science and Technology (Qingdao), 1, Wenhai Road, Aoshanwei, Jimo, Qingdao, 266237, China

[*] Corresponding author. College of Engineering, Ocean University of China, 238, Songling Road, Qingdao, 266100, China. E-mail address: caofeifei@ouc.edu.cn

Abstract

Hybrid wind-wave systems combining the wave energy converters (WECs) with offshore wind turbines (OWTs) is a promising way to enhance the power production and improve the sea space utilization. In this paper, a novel hybrid wind-wave conceptual system, in which a multi-buoy WEC is integrated with a fixed monopile OWT, is proposed. This is the first concept utilizing multi-buoy WECs and is distinguished from existing hybrid wind-wave systems with a fixed monopile OWT, which integrate a single oscillation water column or a heaving point absorber. To characterize the hydrodynamics associated with the proposed system in operational wave conditions with different directionalities, a potential flow solver with an appropriate power take-off (PTO) model is applied. The results demonstrate a significant buoy-buoy and buoy-monopile hydrodynamic interaction, suggesting that the existing hydrodynamic characteristics for the wind-wave system with a single buoy WEC may not be applicable to the new system. More importantly, the power performance of the present system is proven to be better than the corresponding single-buoy wind-wave system, as being quantitatively assessed by the newly-defined evaluation index within the range of the consideration of this paper.

Keywords: wave energy converter; offshore wind turbine; hybrid wind-wave system; numerical simulation; hydrodynamic characteristics

1. Introduction

Ocean energy, including offshore wind, wave, tidal, marine currents, salinity gradients, is abundant and has great potential for harvesting. To achieve the Net-Zero target, the research and development (R&D) of techniques for harvesting ocean energy has become a common strategy of many countries in the world. The offshore wind energy industry has grown rapidly in recent years since the levelized cost of energy (LCOE) of fixed offshore wind farms is competitive with the traditional thermal energy. In addition, harvesting wave energy has also attracted worldwide attention attributing to the high wave energy density. Although plenty of concepts have been developed, wave energy converters (WECs) are generally suffering from a high cost and low reliability, which greatly restrict their commercialization [1]. One feasible approach to cut the cost of the WECs is to share the marine space with the offshore wind turbines (OWTs). Consequently, it increases the energy output per square meter and improves the marine space utilisation [2]. This is justified by two facts, i.e. (1) the OWTs are often grouped as a farm and an operational spacing of 6 ~ 10 times of the turbine diameter is commonly applied in order to minimize the wake interaction [3]. There is plenty of space in the wind farm to accommodate the WECs; (2) the offshore wind and wave resources are highly correlated and offshore wind sites often have abundant wave resources. The cost of WECs can be cut by sharing the infrastructures, including the foundations, cables, and substations with OWTs, as well as operation and maintenance activities [4]. This drives recent R&D on the wind-wave hybrid system that has shown other benefits compared with the OWTs, including a smoother power output [5]. Different types of WECs have been proposed to be combined with OWTs with floating or fixed foundations.

Recent literatures have reported the integration of WECs with three commonly seen floaters, i.e. semi-submersible, spar and tension leg platform (TLP), of the floating OWTs. One typical concept is the integration of the semi-submersible OWT with a point absorber WEC [6], a heave-type torus WEC [7,8] that is installed on the central column of the platform, four torus-shaped WECs [9], multiple heaving WECs [10,11], three WaveStar WECs [12], or twelve cone shape WECs [13]. Generally speaking, these existing works do not only demonstrate the feasibility of the hybrid wind-wave system on increasing the overall power output but also reveal the critical role of WECs in reducing the wave loading on the floaters and stabilizing the floating systems. Similar observations and conclusions have been reported from the hydrodynamic analysis on the hybrid wind-wave system coupling the Spar-type floating OWTs with an axis-symmetric two-body WEC (referred to as the STC system) [14-20] or a heaving buoy WEC [21]. In addition, they also found that the WECs may increase the extreme values of the wave loading [15] and the nonlinear phenomena, such as water entry and exit, green water on deck and Mathieu instability, may become more important [17,18,20] under extreme conditions. Additionally, Ren et al.

[22] and Rony et al. [23] studied a hybrid system integrating a heaving-type point absorber WEC with a TLP-based OWT. They confirmed that the introduction of WECs reduces the motion amplitudes of the TLP. It is noted that the WECs adopted in the hybrid systems indicated above are all point absorbers. Attempts have also been made to combine the oscillating water column WECs with floating OWTs, as reviewed in our previous paper [24]. For all floating hybrid systems, the motions of the WECs and OWTs in the hybrid system depend on each other and are mutually coupled with the complex marine environment. This challenges the system reliability, optimization and control of the floating hybrid system.

Compared with the floating hybrid system, the degree of the complexity of the fixed hybrid system, which integreates the WECs with bottom-fixed OWTs, is significantly reduced, due to negligible motion responses of the WEC foundations. However, the relevant research is not as popular as the floating hybrid system in recent years, despite the fact that the majority of the existing operational wind farms are sitting in the water depth below 30–35 m and adopt bottom-fixed monopile foundations [25]. Ren et al. [26] proposed one hybrid system integrating a heave-type WEC with a monopile foundation of an OWT, and is followed by Homayoun et al. [27], who tried four different shapes of the heaving buoy and investigated the effects of the geometry of the heaving buoy on the hydrodynamic performance. Khatibani and Ketabdari [28] proposed another hybrid system integrating two pitching WECs with an OWT monopile foundation and concluded that the onboard WECs can bring 26.44% extra power. Gkaraklova et al. [29] investigated the performance of a circular array of four semi-submersed heaving WECs distributed uniformly around a monopile foundation and concluded the critical roles of the radial distance from the WECs to the monopile and the power take-off (PTO) characteristics on the power absorption. In addition to the point absorber WECs, OWCs have also been used in the fixed wind-wave system, as demonstrated by Perez-Collazo et al. [30], Zhou et al. [31], Cong et al. [32], Li et al. [1].

Almost all recent development of the hybrid system targets 5-MW OWTs. Following the up-scaling trend, the OWTs have a bigger size and are deployed in deeper water. If a torus-shaped WEC is integrated with the monopile-supported OWTs, as proposed by Ren et al. [26], the size of the WEC increases following the up-scaling of the OWTs. This means that the OWTs and the integrated torus-shaped WECs are exposed to relatively shorter waves, compared with their dimension. Consequently, the radiation/diffraction effects of the WECs become more significant. In this paper, a novel wind-wave system is proposed to integrate an offshore monopile wind turbine with a multi-buoy WEC, which consists of three identical buoys surrounding the monopile. Geometrically, the multi-buoy WEC looks like a torus-shaped WEC being evenly divided into three. However, they can move independently and are subjected to individual power-take-off systems (PTOs). The hypothesis of this concept is that each buoy is subjected to less damping and thus has a more significant motion response compared with the corresponding torus WEC. For a specific PTO, the multi-buoy WEC is expected to produce more power. However, the complex interaction between the buoys and between the OWT and the WECs demands a systematic investigation in order to confirm the hypothesis and to optimise the design for maximising the power performance.

Both experimental and numerical approaches have been used for evaluating the performance and survivability of hybrid systems. Typical examples of experimental studies on the hybrid system include Kamarlouei et al.[13,33] , Wan et al. [17,20] and Ren et al. [26]. Generally speaking, model tests considering extensive cases for the design and optimization is exhausting and costing. It is mainly used to quantify physical phenomena, such as the nonlinear and viscous effects [18,20], and/or to validate the numerical models. In the aspect of numerical simulation, the high-fidelity computational fluid dynamics (CFD) tools are able to resolve small- to micro-scale fluid-structure interaction, turbulence, aeration, and breaking wave impact. However, they are time-consuming and therefore are practically prohibited for design and optimization. CFD modeling is also mainly used to calibrate the simplified models or reduced-order simulations, e.g. to quantify the viscous damping coefficient. The majority of the numerical work on hybrid wind-wave system development employs the potential theory in the time and/or frequency domains, e.g. ANSYS-Aqwa [6-8,12,22,26,28], SIMORIFLEX [9], WAMIT [10,29]. In addition to the use of single potential solvers listed above, there is also numerical work employing different potential solvers for time-domain and frequency-domain analysis. Muliawan et al.[14,15] and Ren et al. [16] applied HydroD for the frequency domain analysis and a combination of SIMO and TDHMILL (Thrust-Dynamic-Horizontal-Mill) for the time domain hydro- and aerodynamic analysis. Wan et al. [19] used the Sesam/Wadam for the frequency domain analysis and SIMO for the time-domain analysis. Zhao et al. [21] used ANSYS-Aqwa and Orcaflex for the frequency- and time-domain analysis, respectively.

Following the state-of-the-art recent development, we adopt the ANSYS-Aqwa to carry out the numerical analysis of the proposed hybrid system in this paper. In the potential theory, the fluid is assumed to be inviscid, and therefore the viscous effects cannot be directly modeled. As in many existing literatures [21,22,26-29], the viscous effect is not included, although it may be taken into account by adding an artificial viscous term in the motion equation of the floating bodies [9-12,14,15]. Compared with CFD, the potential theory considers the hydrodynamic effects on structures and divides the wave force into wave exciting force and radiation force. Analysing different sources of forces can better explain the hydrodynamic mechanism. Thus, more targeted solutions can be provided in the conceptual design process. This well fits the main aim of the present research, i.e. to prove the concept of the proposed hybrid wind-wave system integrating the multi-buoy WEC with a fixed monopile-supported OWT, and to advance the understanding of the hydrodynamic interaction and power performance of the proposed system. This builds the basis of our CFD and experimental research scheduled in the near future, through which the viscous effects can be quantified. The paper is structured as follows. Section 2 presents the details of the wind turbine, monopile, multi-buoy WEC, and wave environmental conditions. Section 3 briefly introduces the numerical models and the motion equation of buoys. The results are then presented and discussed in Section 4. Finally, Section 5 summarizes the conclusions of this study.

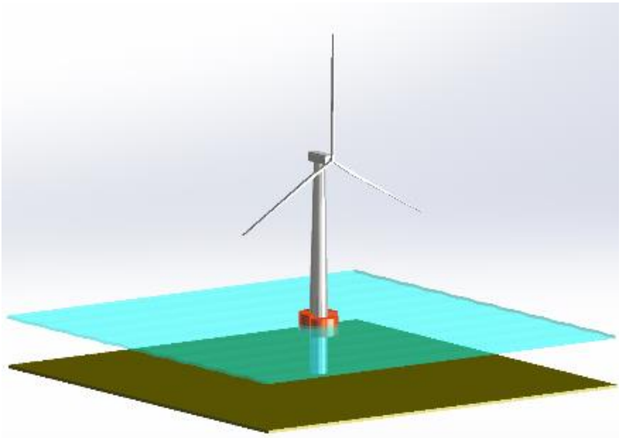

Fig. 1 Concept of the multi-buoy WEC integrated with a monopile-supported OWT

Table 1 Wind turbine's geometric and mass properties [35]

Parameter	Value	Units
Power rating	15	MW
Number of blades	3	-
Cut-in wind speed	3	m/s
Rated wind speed	10.59	m/s
Cut-out wind speed	25	m/s
Rotor diameter	240	m
Hub height	150	m
Blade mass	65	t
Rotor mass	1017	t

2. Configuration of hybrid wind-wave system

The National Renewable Energy Laboratory (NREL) IEA 15 MW reference wind turbine with a bottom-fixed monopile foundation is applied as the porotype in the proposed concept. This work focuses on the hydrodynamics of the OWT and the hybrid systems with single- or multi-buoy WECs, the aerodynamics of the blade, hub and tower are ignored. The numerical model only include the monopile foundation, which is placed at the water depth of 30 m. The diameter of the monopile is 10 m and the transition piece height is 15 m above the mean sea level (MSL). Tables 2 show the geometric and mass properties of monopile foundation.

Table 2 Geometric and mass properties of the foundation [35]

Parameter	Value	Units
Monopile embedment depth	45	m
Water depth	30	m
Transition piece height	15	m
Monopile base diameter	10	m
Monopile mass	1318	t

The multi-buoy WEC in the proposed hybrid wind-wave system is derived from the torus-shaped buoy, which has been attempted to be integrated into the monopile OWT [24,26]. In the present study, we divide the torus-shaped buoy into three identical buoys that are evenly installed surrounding the monopile. Fig. 2 illustrates the concept of the multi-buoy WEC and the monopile, where the tower, hub and blade are not modelled as described above. Table 3 summarises the geometric properties of the multi-buoy WEC. On each buoy, a independent PTO system is installed. Both the linear and coulomb PTO models [21] will be considered in the present numerical investigation. Buoys are configurated to be moved vertically along the linear guide-roller system which is fixed on the monopile and captures wave energy through the heave motion.

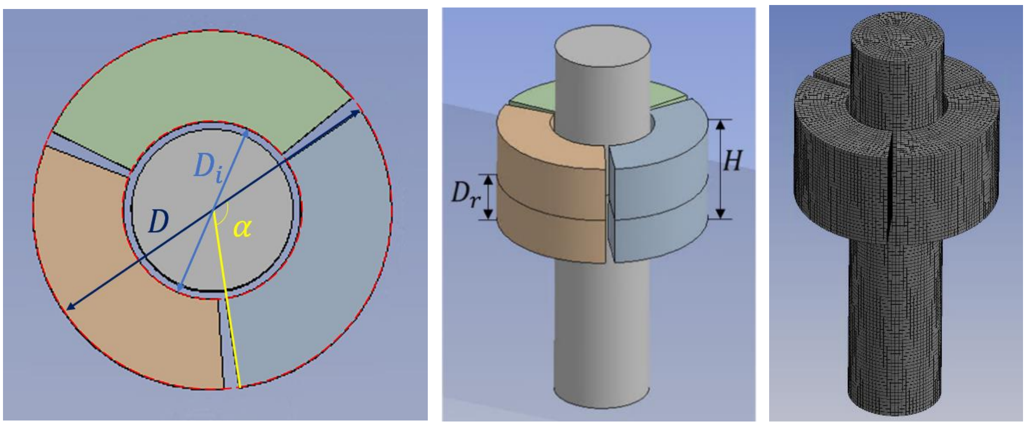

(a) The top view **(b) 3D view** **(c) computational mesh**

Fig. 2 Illustrations of the hybird system and an example of the computational mesh

Table 3 Geometric properties of the WEC

Parameter	Value	Units
Outer diameter (***D***)	22	m
Inner diameter (***D**$_i$*)	11	m
Circular gap thickness	0.5	m

Height (***H***)	11	m
Central angle of Buoy (***α***)	115	degrees
Gap between Buoy	5	degrees
Draft (***D_r***)	4.5	m
Centre of gravity of Buoy above MLS	1	m

Table 4 The values of *kh* and *kD* corresponding to *T*

***T*(s)**	**3**	**4**	**5**	**6**	**7**	**8**
kh	13.42	7.55	4.83	3.37	2.50	1.96
kD	9.85	5.54	3.55	2.47	1.83	1.44

According to the statistics of the marine environments near Shandong province in China [11], the characteristic wave period *T* varies from 3 s to 8 s. Table 4 shows the values of *kh* and *kD* corresponding to different values of *T*, where *k* is the wave number. With the water depth *h* of 30 m, *kh* ranges from 1.96 to 13.42, covering both the finite-depth and deep-water waves. The corresponding range of *kD* is 9.85 ~ 1.44, beyond the range of the application of Morison's equation, i.e. $kD < 1.26$ ($D/\lambda < 0.2$ where λ is the wavelength). This suggests the interaction between the wave and the wind-wave system falls into the diffraction zone and the viscous effect may be neglected. In this paper, we focus on the operational condition and therefore the wave heights of 0.5 m and 1.0 m are used for assessing the dynamic responses without PTO forces and the power performance of the system with PTO forces, respectively. The maximum wave steepness *kA* is approximately 0.22 for $T = 3$ s where *A* is the wave amplitude and thus Stokes 2^{nd} or third order theory is sufficient to describe the incident wave. With such wave conditions and the characteristic dimension (the outer diameter of the buoy), the maximum value of Keulegan-Carpenter number (*KC)* is approximately 0.14 and the Reynolds number *Re* ranges from 8.55 to 22.81×10^6. These imply insignificant wave separation ($KC < 1$) and viscous effects ($Re > 10^6$). It shall be noted that the hybrid system involves multiple bodies and the gap resonance may occur. When the gap resonance happens and/or the wave frequency is close to the natural frequency of the buoys, the potential theory may over predict the motion of the floating bodies if the viscosity is not considered. However, the associated viscous effect is linear and ignoring it does not influence the qualitative conclusion [34].

3. Methodology

In this work, the hydro- and aero-elasticity of the structure are ignored, and the WEC and the monopile of the wind-wave hybrid system are modeled as rigid bodies. The seabed is simplified as a flatbed. The monopile is set to be fixed by a rigid joint that connects the central point of the bottom of the monopile to a fixed point at the seabed. The WEC is restricted to have one degree of freedom in heave. A three-dimensional full-scale numerical model is built in ANSYS-Aqwa and an example of the computational mesh is shown in Fig. 2(c).

In the first stage of the simulation, a frequency-domain analysis is conducted using ANSYS-Aqwa to compute the hydrodynamic load/coefficients on floating or fixed rigid bodies by employing linearized three-dimensional radiation/diffraction theory where the interaction between different bodies can be considered. After the hydrodynamic coefficients (radiation and diffraction) are obtained using the frequency domain analysis, a time-domain simulation is followed. The memory effect of the radiation force is taken into account through the convolution approach in the time domain. The motion equation of the heaving buoy can be expressed as:

$$m\ddot{x} = F_e + F_r + F_c + F_{PTO} - Rx \tag{1}$$

where m is the mass of the heaving buoy; x is the displacement of the buoy; F_e is the wave exciting force; F_r is the radiation force that is is caused by the disturbed waves induced by the body motion; F_c is the frictional resistance between the heaving buoy and the monopile, which is neglected not only because the linear guide-roller system has a very low friction effect, but also for the full-scale model, the friction is relatively small compared with the wave loads on the buoy; F_{PTO} is the PTO force and R is the hydrostatic stiffness coefficient of the buoy. The wave exciting force consists of the Froude-Krylov force, which is induced by the undisturbed incident wave, and the diffraction force, which is induced by the disturbance wave due to the existence of the structure, i.e. the heaving buoy herein. For the single-DOF heaving buoy, R can be calculated using

$$R = \rho g S \tag{2}$$

where S is the cut water-plane area of the buoy, ρ is the water density and g is the gravitational acceleration. For the case involving three heaving buoys and a fixed monopile, by ignoring the wind loads and the frictional resistance, the heaving motions of three buoys can be calculated by

$$\begin{bmatrix} \left(m_1 + A_{11}(\infty)\right) & A_{12}(\infty) & A_{13}(\infty) \\ A_{21}(\infty) & \left(m_2 + A_{22}(\infty)\right) & A_{23}(\infty) \\ A_{31}(\infty) & A_{32}(\infty) & \left(m_3 + A_{33}(\infty)\right) \end{bmatrix} \begin{bmatrix} \ddot{x}_1(t) \\ \ddot{x}_2(t) \\ \ddot{x}_3(t) \end{bmatrix} + \int_0^t \begin{bmatrix} k_{11}(t-\tau) & k_{12}(t-\tau) & k_{13}(t-\tau) \\ k_{21}(t-\tau) & k_{22}(t-\tau) & k_{23}(t-\tau) \\ k_{31}(t-\tau) & k_{32}(t-\tau) & k_{33}(t-\tau) \end{bmatrix} \begin{bmatrix} \dot{x}_1(\tau) \\ \dot{x}_2(\tau) \\ \dot{x}_3(\tau) \end{bmatrix} d\tau + \begin{bmatrix} R_1 & 0 & 0 \\ 0 & R_2 & 0 \\ 0 & 0 & R_3 \end{bmatrix} \begin{bmatrix} x_1(t) \\ x_2(t) \\ x_3(t) \end{bmatrix} = \begin{bmatrix} F_{e1}(t) \\ F_{e2}(t) \\ F_{e3}(t) \end{bmatrix} + \begin{bmatrix} F_{PTO1}(t) \\ F_{PTO2}(t) \\ F_{PTO3}(t) \end{bmatrix} \tag{3}$$

where A_{mn} is the added mass and k_{mn} is the velocity impulse function, which can be obtained by Eq. (4) [37].

$$k_{mn}(t) = \frac{2}{\pi} \int_0^\infty B_{mn}(\omega) \cos(\omega t) \, \mathrm{d}\omega \tag{4}$$

where B_{mn} is the radiation damping. Eq. (3) is an extension of Eq. (1) for the multi-body dynamics. In Eq. (3), the interactions between bodies are included through the added mass and the kernels, which are obtained in the corresponding linear frequency-domain analysis before the time-domain analysis. The wave exciting force F_{em}, m = 1, 2 and 3, are obtained by integrating the incident wave potential and the diffraction wave potential, which are solved by corresponding Laplace equations with specific boundary conditions. For more details of the linear diffraction theory adopted by ANSYS-Aqwa, the readers are referred to the software manual or the paper cited above.

As indicated above, both the linear and coulomb PTO models will be considered in this work. For the former, the PTO force F_{PTO} is proportional to the velocity of the heaving buoy and can be presented as

$$F_{PTO} = -B \cdot \dot{x}(t) \tag{5}$$

where B is the linear PTO coefficient. For the Coulomb PTO model, the PTO force F_{PTO} is calculated using

$$F_{PTO} = -sign\left(\dot{x}(t)\right) \cdot C \tag{6}$$

where the direction of the damping force is always opposite to the velocity and C is a constant. The instantaneous power captured by a buoy can be evaluated by,

$$P(t) = -F_{PTO}\dot{x}(t) \tag{7}$$

and, the mean absorbed wave power during the time nT can be obtained using,

$$P_m = \frac{1}{nT} \int_{t_0}^{t_0+nT} P(t)\,dt \tag{8}$$

where n is the number of wave periods used to evaluate the mean wave power and t_0 is the starting time when the motion of the WEC enters the steady state.

For the convenience of the analysis, the dynamic response of the buoy is represented by the response amplitude operator (RAO),

$$\text{RAO} = \frac{A_b}{A} \tag{9}$$

where A_b is the amplitude of the buoy motion and A is the wave amplitude; the force is nondimensionalized by

$$\overline{F} = \frac{F}{\rho g A D^2} \tag{10}$$

where F is the force's amplitude; the nondimensional linear PTO coefficient $\bar{B}$, Coulomb PTO constant $\bar{C}$ and mean absorbed wave power $\overline{P_m}$ are defined as follows:

$$\overline{B} = \frac{B}{\rho g^{0.5} A D^{1.5}} \tag{11}$$

$$\overline{C} = \frac{C}{\rho g A D^2} \tag{12}$$

$$\overline{P_m} = \frac{P_m}{\rho g^{1.5} A D^{2.5}} \tag{13}$$

The present numerical approach is validated by comparing its numerical prediction with the experimental data available in Ren et al. [26], in which a hybrid wind wave system integrating a torus-shaped buoy with a fixed monopile foundation. The RAO of the heaving buoy, the PTO force amplitude and the mean wave power are considered in the comparison. Detailed case configuration and the comparison can be found in Li et al [24]. For completeness, the key results are duplicated in Fig. 3, which shows a satisfactory agreement between the present numerical results and the experimental data.

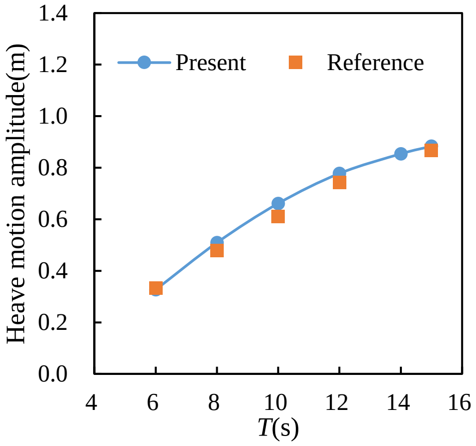

(a) Heave motion amplitude

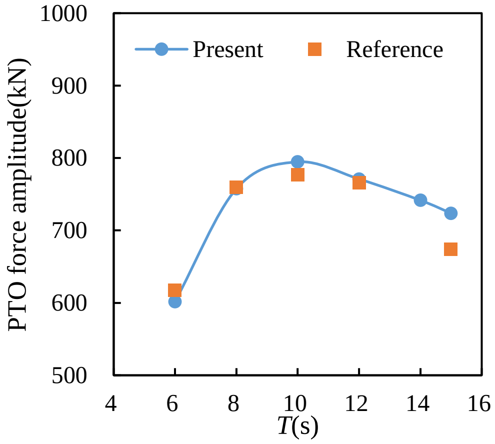

(b) PTO force amplitude

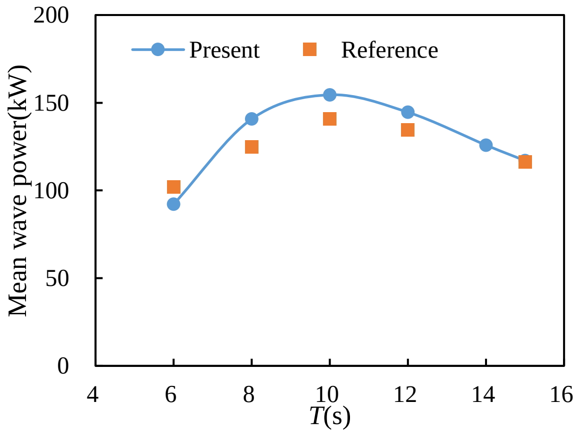

(c) Mean wave power

Fig. 3 Comparison of (a) heaving amplitude, (b) PTO force amplitude and (c) Mean wave power in the cases with different wave periods (wave height is 2 m)

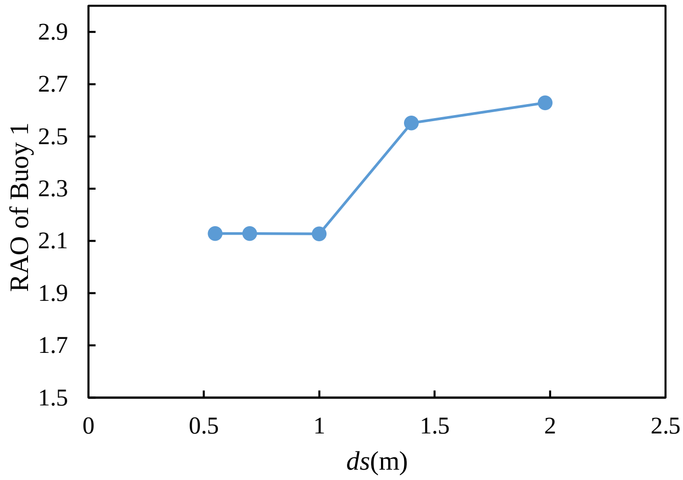

Fig. 4 Heave RAO of Buoy 1 in the cases with different cell sizes (wave height is 0.5 m, wave period is 6 s)

For all cases considered in this paper, convergence tests have been conducted to ensure the reliability of the numerical results. For this purpose, various mesh sizes are employed. Fig. 2(c) shows an example of the computational mesh utilized in the present numerical study, featuring a maximum element size ds of 0.7 m, a defeaturing tolerance of 0.4 m and total cell number of 21,133. The heaving RAO of Buoy 1 is considered as the criteria to assess the convergence. Fig. 4 displays the convergent process for the cases with incident wave height of 0.5 m and wave period of 6 s. The featured mesh size ds ranges from 0.55 to 1.98 m, yielding a total cell numbers ranging from 33,836 to 2,908. As observed from Fig. 4, the RAO of Buoy 1 is convergent to a specific value when $ds \leq 1$ m (total cell number is 10,626). Similar observation is found in other cases and the results are not shown for saving the space.

4. Results and discussion

4.1 Hydrodynamic interaction between buoys

As indicated above, the hydrodynamic interaction between buoys (coupling effects) may be important due to their close proximity in the system. Light is shed to reveal the coupling effects. To do so, two different arrangements of the buoys are considered, i.e. Buoy 1 only, multi-buoy system consisting of 3 buoys. Different incident wave directions, i.e. 0, 120, and 180 degrees are chosen in the investigation. The buoy numbering and the definition of the wave directionality are illustrated in Fig. 5.

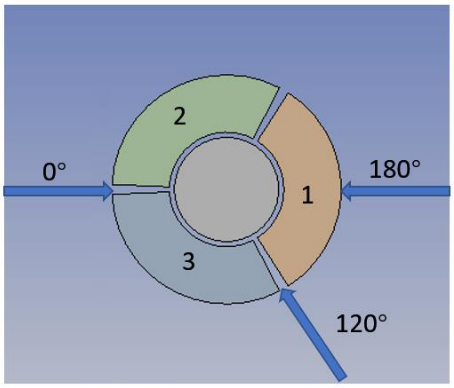

Fig. 5 The definition of three model and wave directions

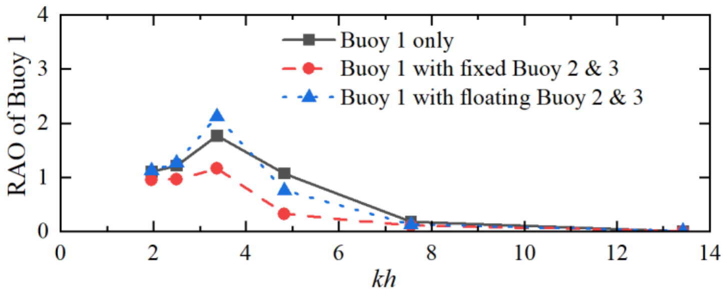

（a）0°

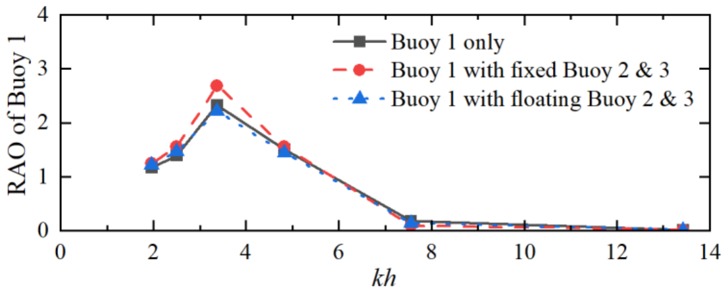

（b）120°

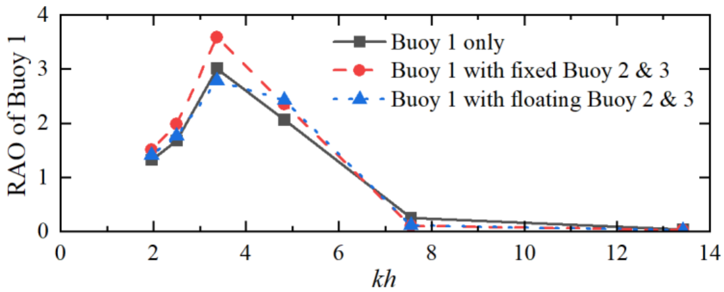

（c）180°

Fig. 6 Heave RAO of Buoy 1 subjected to (a) incident angle of 0°; (b) incident angle of 120° and (c) incident angle of 180° (F_{PTO} = 0 N)

Fig. 6 compares the RAO of Buoy 1 in the cases with different configurations subjected to different wave directionalities. The PTO in these cases is shut and Buoy 1 is subjected a free heaving motion excited by the incident waves. If Buoy 2 & 3 are involved, they may be fixed (marked as Buoy 1 with fixed Buoy 2 & 3) or in a free heaving motion (marked as Buoy 1 with floating Buoy 2 & 3). For all cases, the peak value of the RAO occurs at kh = 3.37, corresponding to the wave period of 6 s which is close to the natural period of the buoy (5.5 s). However, the introduction of the accompanied buoys close to Buoy 1 affects the peak RAO values. For the cases with an incident angle of 0°, Buoy 1 with floating Buoy 2 & 3 has a considerably larger peak RAO compared with that of Buoy 1 only; whereas the appearance of floating Buoy 2 & 3 weakens the peak RAO of Buoy 1 in the case with incident angles of 120° and 180°. When Buoy 2 & 3 are fixed, they provide a shielding effect on the motion of Buoy 1 when the incident angle is 0, whereas significantly amplify the peak value when the incident angle increases. The buoy-buoy interactions also influence the RAO in the cases with other wave frequencies, especially near kh = 3.37. Depending on the wave directionality, it may strengthen or suppress the motion of Buoy 1. This confirms the significance of the buoy-buoy interaction, i.e. the coupling effect, in the multi-buoy system proposed here. One may also notice that the RAO of Buoy 1 increases as the incident wave angle increases. It is clearer in Fig. 7 which duplicates the results in Fig. 6 and focuses on the comparison of RAOs in the cases with different incident angles.

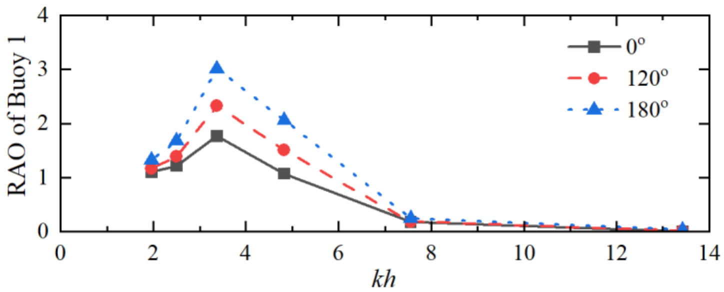

(a) Buoy 1 only

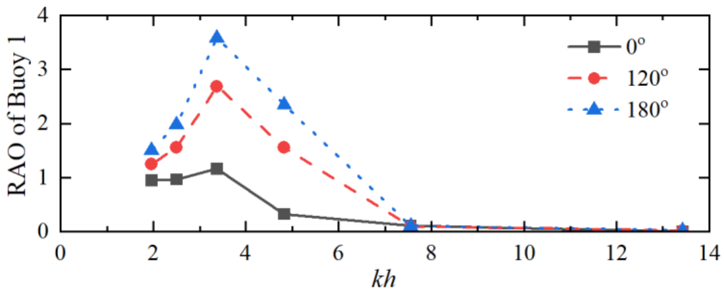

(b) Buoy 1 with fixed Buoy 2&3

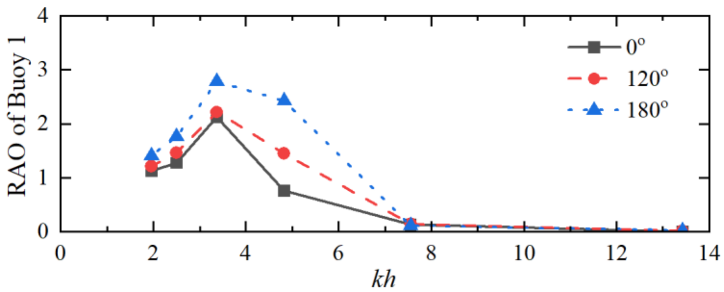

(c) Buoy 1 with floating Buoy 2&3

Fig. 7 Effects of wave directionality on the heave RAO of Buoy 1 for (a) Buoy 1 only; (b) Buoy 1 with fixed Buoy 2 & 3 and (c) Buoy 1 with floating Buoy 2 & 3 (F_{PTO} = 0 N)

Attention is also paid to the force acting on the buoys. For this purpose, the dimensionless total force, diffraction force, Froude-Krylov force and the radiation force in the heaving direction in the cases shown in Fig. 6 and Fig. 7 are analyzed. Results are displayed in Fig. 8, Fig. 9 and Fig. 10 for the cases with the incident angles of 0º, 120º and 180º, respectively. Similar to Fig. 6, results from cases with Buoy 1 only, Buoy 1 with fixed Buoy 2 & 3 and Buoy 1 with floating Buoy 2 & 3 are plotted together for comparison.

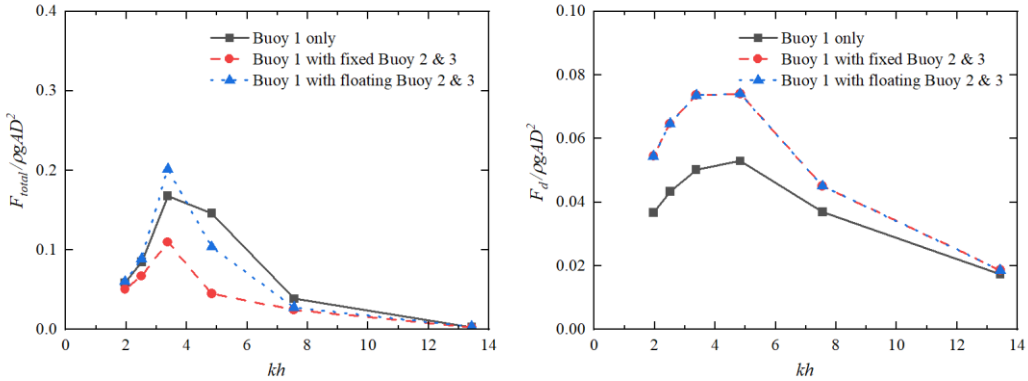

(a)Total force **(b)Diffraction force**

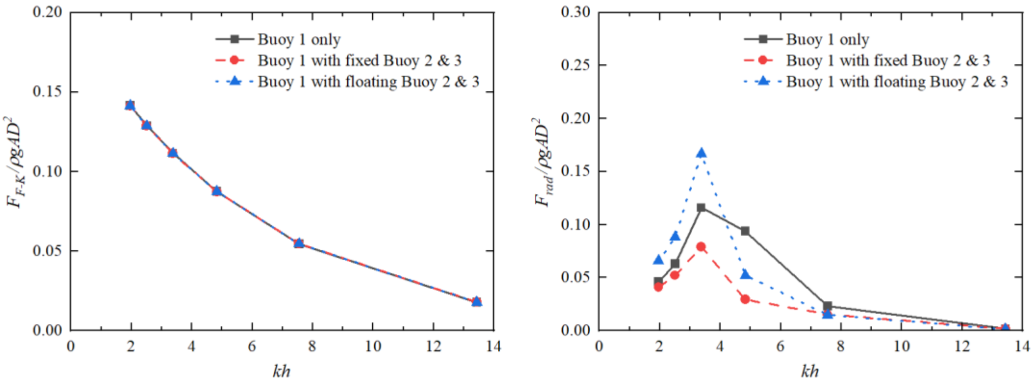

(c)Froude-Krylov force **(d)Radiation force**

Fig. 8 Comparison of (a) total force; (b) diffraction force; (c) Froude-Krylov force and (d) Radiation force on Buoy 1 subjected to incident wave angle of 0 (F_{PTO} = 0 N)

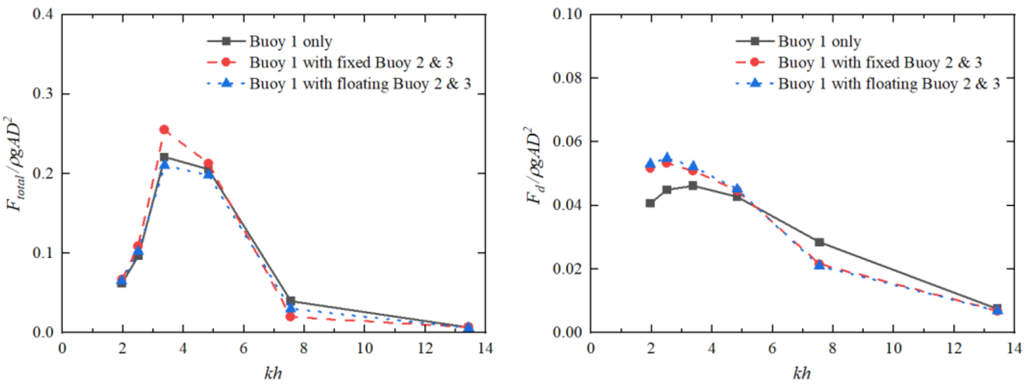

(a)Total force **(b)Diffraction force**

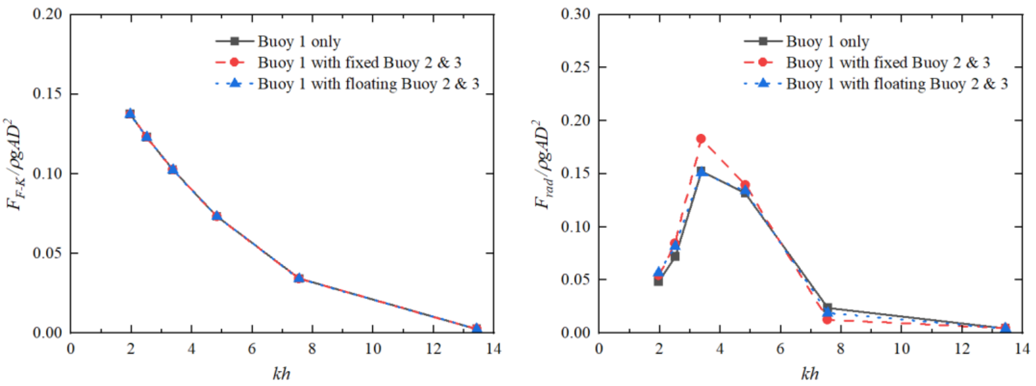

(c)Froude-Krylov force **(d)Radiation force**

Fig. 9 Comparison of (a) total force; (b) diffraction force; (c) Froude-Krylov force and (d) Radiation force on Buoy 1 subjected to incident wave angle of 120° (F_{PTO} = 0 N)

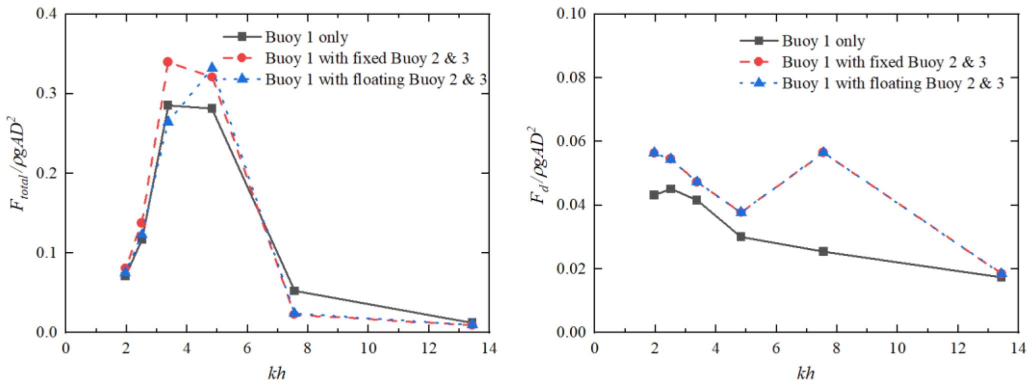

(a)Total force **(b)Diffraction force**

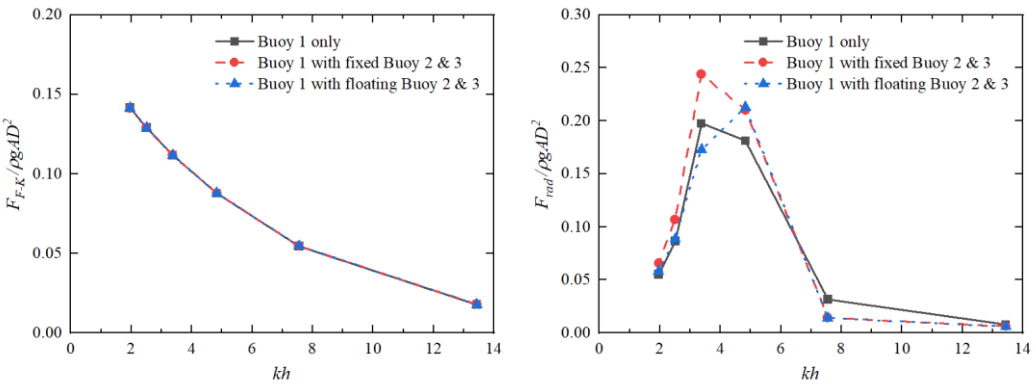

(c)Froude-Krylov force **(d)Radiation force**

Fig. 10 Comparison of (a) total force; (b) diffraction force; (c) Froude-Krylov force and (d) Radiation force on Buoy 1 subjected to incident wave angle of 180° (F_{PTO} = 0 N)

One can observe from Figs. 8(a), 9(a) and 10(a) that the trend of the total force acting on Buoy 1 in terms of *kh* is largely consistent with that of the heave RAO of Buoy 1 shown in Fig. 6. In the linear potential theory, the Froude-Krylov only depends on the incident wave potential and is not affected by the motion of the structure and the appearance of surrounding structures. Therefore, its values in the cases with or without accompanied Buoy 2 & 3 exhibit the same profile (Figs. 8(c), 9(c) and 10(c)). The buoy-buoy interaction mainly affects the diffraction force and the radiation force.

The former is induced by the disturbance wave due to the existence of a structure. For the cases with Buoy 2 & 3 accompanied with Buoy 1, the diffraction force of Buoy 1 remains unchanged when Buoy 2 & 3 are in free heaving motion compared to when Buoy 2 & 3 are fixed, for any specific value of kh. For the incident wave angle of 0° (Fig. 8(b)) and 180° (Fig. 10(b)), the appearance of Buoy 2 and 3 amplifies the diffraction force within the whole range of frequency considered in this work; for the incident angle of 120° (Fig. 9(b)), Buoy 2 and 3 amplify the diffraction force on Buoy 1 when $kh \leq 5$ but suppress it afterward. The radiation force is induced by the motion of the structure. Consequently, its trend in terms of kh is consistent with the trend of the RAO of and the total force acting on Buoy 1.

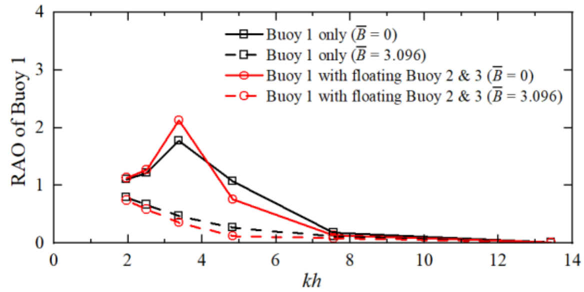

(a) 0°

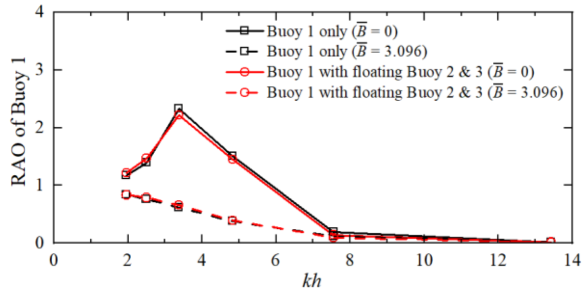

(b)120°

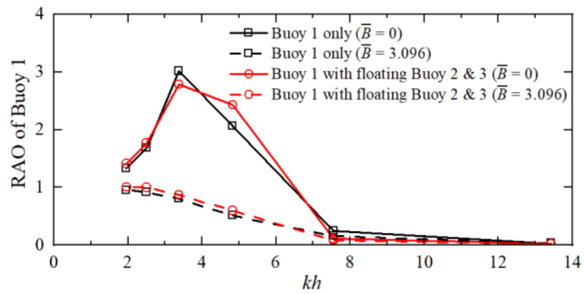

(c)180° Fig. 11 Heave RAOs of Buoy 1 with and without PTOs subjected to (a) incident angle of 0°; (b) incident angle of 120° and (c) incident angle of 180°

In addition to the investigation on free-heaving buoys without the PTO, cases with PTO are also considered to reveal the coupling effects of buoys. To do so, each buoy in the system is subjected to a separated but identical PTO system. The PTO force is calculated using Eq. (5). Fig. 11 shows the heave RAOs of Buoy 1 with and without accompanied Buoy 2 & 3 subjected to different wave directionalities. The nondimensional linear PTO coefficient $\overline{B}$ of 3.096 is used in the cases with PTO for demonstration. More values of $\overline{B}$ will be utilised in the systematic investigation presented in the following section. For the purpose of comparison, both the results with and without PTOs are plotted together. It clearly shows that the application of PTO suppresses the heave motion of buoys. For the cases with the same PTO coefficients, the appearance of Buoy 2 & 3 suppresses the motion of Buoy 1 when the incident angle is 0° but amplifies the motion of Buoy 1 when the incident angle is 180°, compared with the results with Buoy 1 alone. For the incident angle of 120°, Buoy 2 & 3 seem not to considerably affect the motion of Buoy 1.

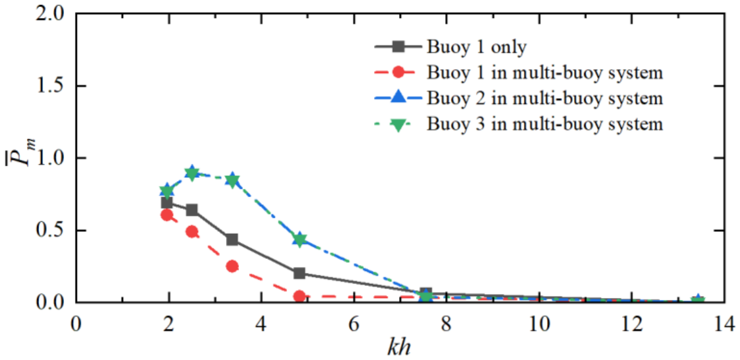

(a) 0°

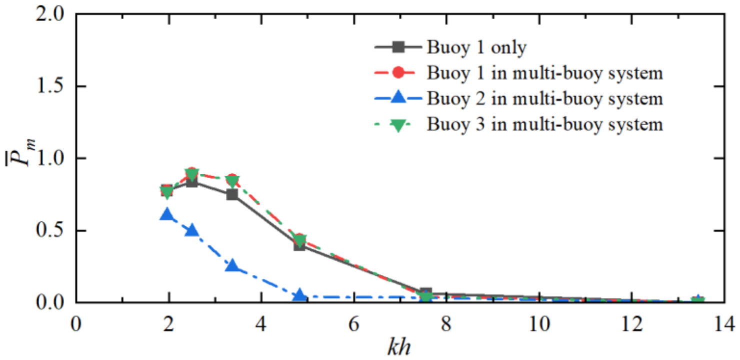

(b) 120°

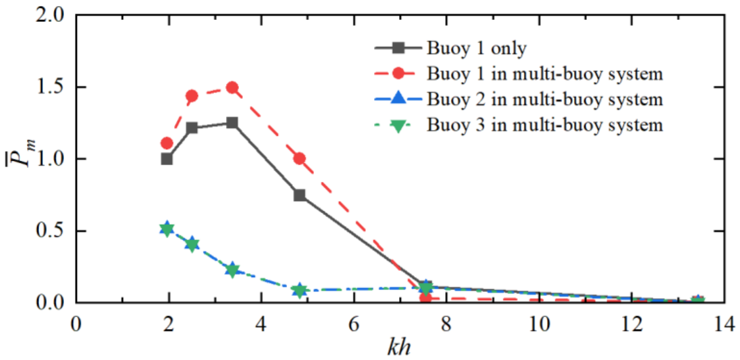

(c) 180°

Fig. 12 Absorbed power by buoys subjected to (a) incident angle of 0°; (b) incident angle of 120° and (c) incident angle of 180° ($\overline{B}$ = 3.096)

The corresponding power absorbed by buoys in the cases shown in Fig. 11 is plotted in Fig. 12. For the cases involving Buoy 1 with Buoy 2 & 3 (marked as multi-buoy system in Fig. 12), the absorbed powers by all buoys are plotted for comparison. In the low-frequency region (kh < 7.55), the introduction of Buoy 2 & 3 increases the absorbed power by Buoy 1 when the incident angles are 120° (Fig. 12(b)) and 180° (Fig. 12(c)); whereas it reduces the power absorbed by Buoy 1 when the incident angle is 0°. In the high-frequency region ($kh > 7.55$), the absorbed power in all cases is very low, although the introduction of Buoy 2 & 3 affects the power absorption of Buoy 1. It shall be pointed out that for the multi-buoy system, all buoys absorb the wave power, as illustrated in Fig. 12. When the incident angle is 0°, although the absorbed power by Buoy 1 in the multi-buoy system is lower than the corresponding value when Buoy 1 is placed alone, the power absorbed by Buoy 2 and 3 are much higher (Fig. 12(a)). Therefore, the power performance of multi-buoy system will be evaluated by considering the total power absorptions from three buoys in the following Section.

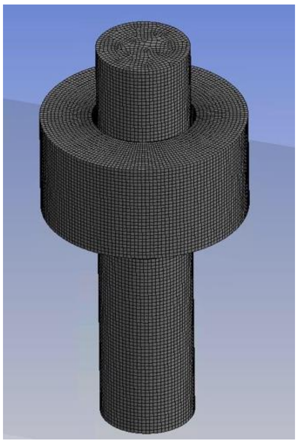

Fig. 13 Numerical model for the sing-buoy WEC integrated into the monopile

4.2 Superiority in power performance of the multi-buoy WEC

The preliminary assessment on the hydrodynamics associated with the multi-buoy system in the previous section reveals a significant role of the coupling effects between buoys and the monopile. For a specific buoy, i.e. Buoy 1 in Section 4.1, the other buoys in the multi-buoy system bring considerable influence on the motion response (i.e. the heave RAO), the force and the power absorptions. This section responds to the main research question of this work and confirms the hypothesis of the proposed concept, i.e. whether the multi-buoy WEC performs better than the corresponding torus-shaped buoy (referred to as single-buoy WEC in the rest of the paper) that has the geometry (height, draft, inner and outer diameter), motion property (mass) and the PTO being equivalent to the summation of three buoys in the present concept. As for multi-buoy WEC, the absorbed power is obtained by summing the power of each buoy. The torus-shaped buoy integrated with the fixed monopile OWT has been experimentally and numerically investigated by Ren et al [26]. In Li et al [24], the torus-shaped buoy is up-scaled to be integrated with a larger scale OWT with a fixed monopile foundation (IEA 15 MW), which is illustrated in Fig. 13 and corresponds to the present concept (Fig. 2(b)). For the purpose of comparison, an evaluation index I_E is proposed to represent the difference in the energy capture characteristics of the multi-buoy WEC and the corresponding single-buoy WEC,

$$I_E = \frac{\sum_{i=1}^{n} P_i - P_S}{\max(P_S)} \tag{13}$$

In which, P_S is the absorbed power of the single-buoy WEC; P_i is the absorbed power of *i*-th buoy of the multi-buoy WEC (i = 1, 2, 3); n = 3 is the number of buoys in the multi-buoy WEC; $\sum_{i=1}^{n} P_i$ is the total power of the multi-buoy WEC obtained by summing the power of each buoy. If I_E is positive, the power performance of the multi-buoy WEC is better than the single-buoy WEC, and the value indicates the increase of the multi-buoy power over the maximum power of the single-buoy under specific conditions; if I_E is 0, the absorbed power of both is the same; if I_E is negative, the power performance of the single-buoy is better than that of the multi-buoy WECs. In order to maximize the range of the application, both the linear (Eq. 5) and Coulomb PTO (Eq. 6) models are implemented in the numerical investigation.

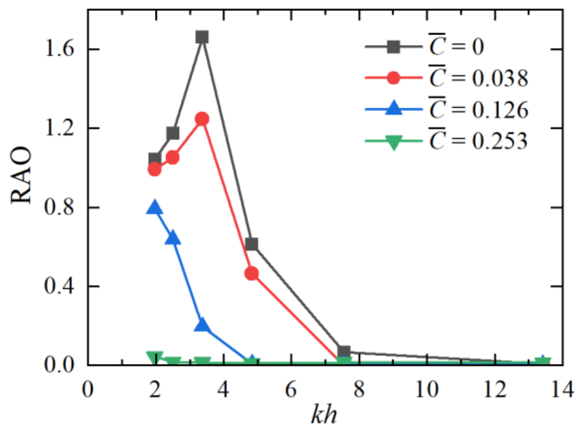

Fig. 14 Heave RAO of the single-buoy WEC in the cases with different Coulomb PTO constant (incident angle of 0°)

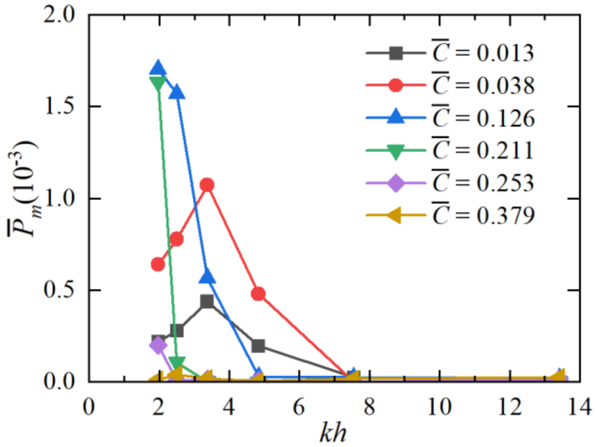

Fig. 15 Absorbed power of the single-buoy WEC in the cases with different Coulomb PTO constant (incident angle of 0°)

Fig. 14 and Fig. 15, respectively shows the heave RAO and the absorbed power of the single-buoy WEC in the cases with different wave frequencies and nondimensional Coulomb PTO constant ($\bar{C}$). As expected, the RAO of the buoy decreases as the PTO damping increases; when $\bar{C}$ = 0.253, the motion response of the buoy becomes negligible (Fig. 14), yielding a negligible power absorption (Fig. 15). It is also found from Fig. 14 that the increase of PTO damping seems to shift the occurrence of the peak RAO towards lower frequency (smaller *kh*). A similar phenomenon on shifting the occurrence of peak value by increasing the PTO damping is observed in Fig. 15. This implies that the natural (resonance) frequency of the single-buoy WEC decreases as the increase of the coulomb PTO damping. The peak value increases as the PTO damping increases up to 0.126. For $\bar{C}$ > 0.126, the hump – shaped peak value is not observed in the frequency range, although one may envisage that such peak occurs at *kh* < 2 which exceeds the present frequency range. When $\bar{C}$ is larger than or equal to 0.379, a single buoy cannot capture wave energy in the current wave frequency range, and neither does the corresponding multi-buoy WEC when the PTO forces of three buoys are all 0.126 in Fig. 16.

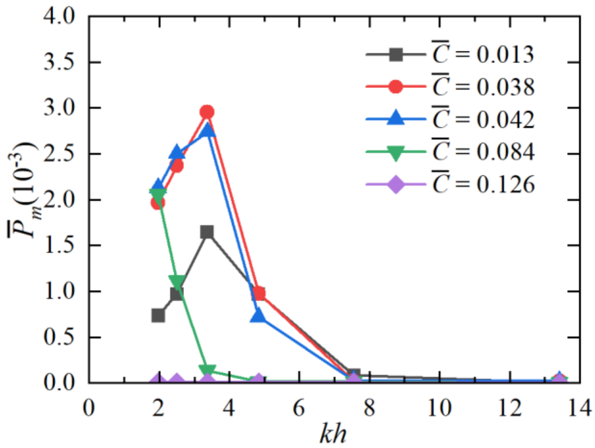

Fig. 16 Absorbed power of multi-buoy versus wave frequency *kh* with 0° wave direction and different PTO forces

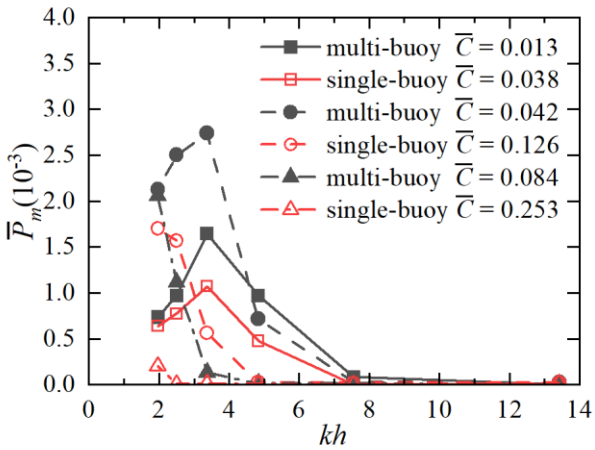

Fig. 17 Comparison of absorbed power between the single-buoy WEC and multi-buoy WEC with 0° wave direction

However, when a smaller PTO damping is applied, the variation of PTO results in a different feature of power variation for the multi-buoy WEC. One feature is that the occurrence of the peak value (corresponding to the resonance frequency, i.e. approximately kh = 3.37) is not sensitive to the change of PTO when the total PTO damping $\bar{C} \leq 0.126$. This provides a great benefit on securing a satisfactory statistic of the power production in real sea. It shall be noted that the range of periods of 3 – 8 s is considered in this work but the probability of the occurrence of wave near the boundary of the range ($T \approx 8$ s, $kh \approx 2$) is low. Consequently, the probability of the occurrence of peak power is low. One may also find that the mean power from the multi-buoy WEC is higher than that of the single-buoy WEC with the same PTO force. It is clearer in Fig. 17 which compares the absorbed power between the single-buoy WEC and the multi-buoy WEC. From Fig. 17, it is observed that the power performance of the multi-buoy WEC is better than the single-buoy WEC in the cases where WECs can capture wave energy; for specific PTO, the peak value of the absorbed power from the multi-buoy WEC occurs at a higher frequency, compared with the single-buoy WEC, implying that the multi-buoy WEC is more suitable for absorbing power at smaller wave periods (higher kh).

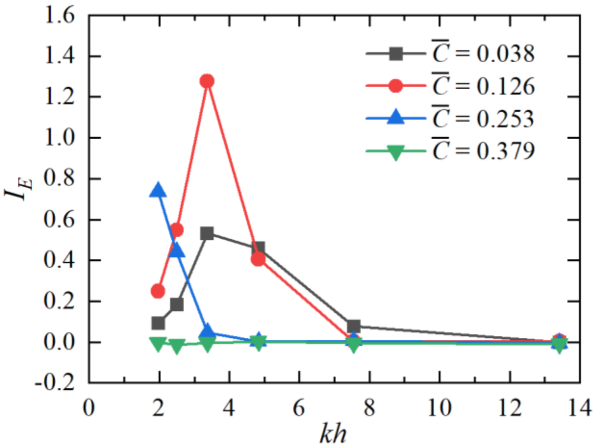

Fig. 18 The indicator I_E versus kh under different coulomb PTO forces

The indicator I_E can reveal the relationship of the absorbed power between those two WECs quantitively. Some results are shown in Fig. 18. It can be observed that I_E has a nonlinear relationship with kh and coulomb PTO constant; there are optimal kh and PTO coefficients, which make the energy-increasing effect of the multi-buoy WEC the most significant. In the present study, this effect is achieved when kh is 3.37 and nondimensional coulomb PTO constant $\bar{C}$ is 0.126, and the absorbed power of the multi-buoy WEC is nearly 1.3 times higher than that of the single-buoy WEC. Overall, multi-buoy WEC has advantages over single-buoy WEC in capturing wave energy under the current wave and PTO condition.

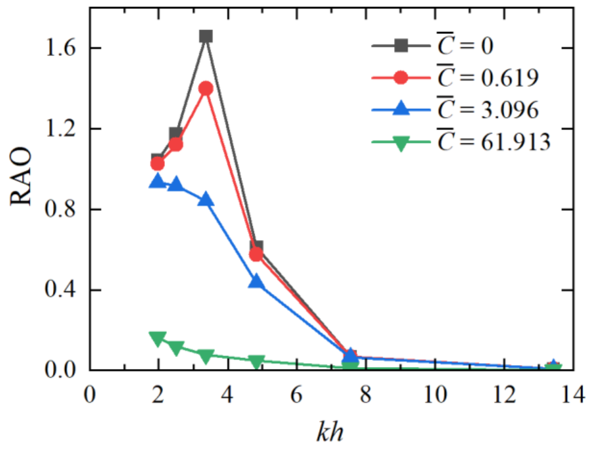

Fig. 19 Heave RAO of the single-buoy WEC in the cases with different linear PTO coefficients (incident angle of 0°)

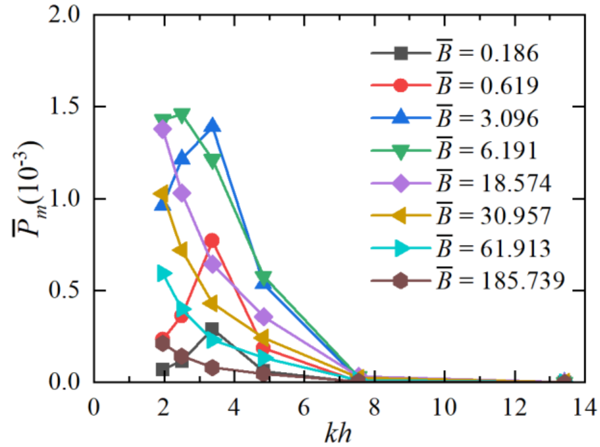

Fig. 20 Absorbed power of the single-buoy WEC versus wave frequency *kh* under different linear PTO coefficients

Linear PTO is also taken into account in the work. Fig. 19 and Fig. 20, respectively, display the heave RAO and absorbed power of the single-buoy WEC. Similar to Fig. 14, Fig. 19 once again shows the reduction of the heave RAO following the increase of the PTO. However, the variation of the power performance (Fig. 20) with linear PTO is different from that with Coulomb PTO. When $\bar{B}$ increases from 0.186 to 3.096, the peak value of the absorbed power occurs at a higher frequency (*kh*) and the peak value increases. When $\bar{B}$ increases further, the peak value occurs at a lower frequency that is beyond the range of the wave frequency considered in this work. The power performance of the multi-buoy WEC with a linear PTO is presented in Fig. 21, which exhibits a similar trend of variation to the corresponding single-buoy WEC. Nevertheless, the superiority of the multi-buoy WEC over the single-buoy WEC is not clearly observed from this figure.

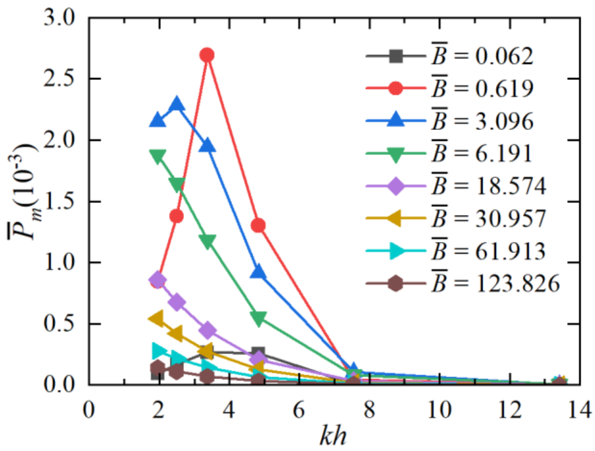

Fig. 21 Absorbed power of multi-buoy WEC versus wave frequency *kh* with 0° wave direction and different linear PTO coefficients

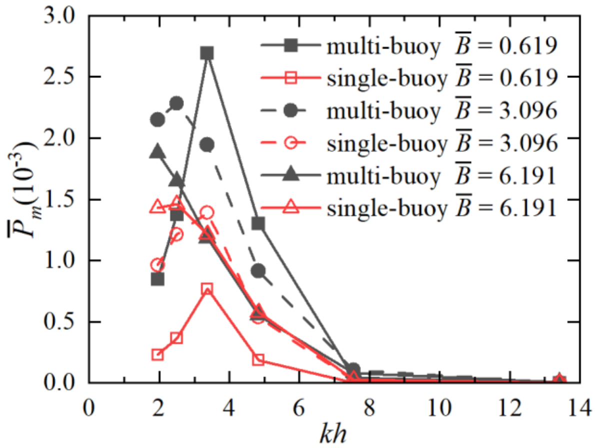

(a) the nondimensional linear PTO coefficient $\overline{B}$ is less than 18.574

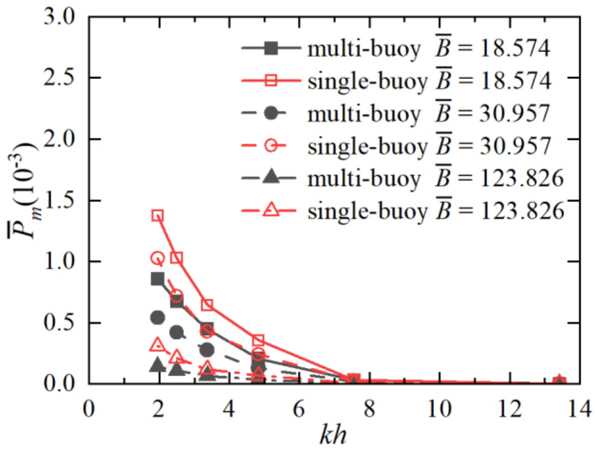

(b) the nondimensional linear PTO coefficient $\overline{B}$ is more than 18.574

Fig. 22 Comparison of absorbed power between the single buoy and multi-buoy with 0° wave direction and different total PTO coefficient

In order to figure out the difference between a single-buoy WEC and a multi-buoy WEC in capturing energy, comparisons of absorbed power between these two systems with a 0° wave direction are presented in Fig. 22. The linear PTO coefficient of the single-buoy WEC is the same as that of each buoy in the multi-buoy WEC. It is clear that when $\bar{B}$ is less than 6.191 (Fig. 22 (a)), the absorbed power of the multi-buoy WEC is more than that of the single buoy; when $\bar{B}$ is higher than 18.574, the absorbed power of the single buoy is higher. Combined Fig. 22(a) and (b), it is easy to find that the highest power is captured by the multi-buoy WEC at *kh* 3.37.

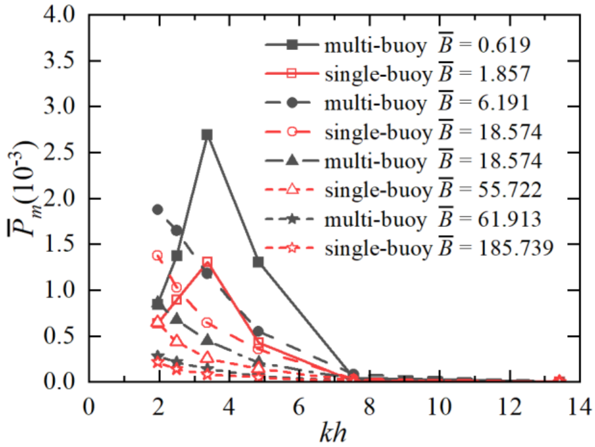

Fig. 23 Comparison of absorbed power between the single buoy and multi-buoy with 0° wave direction and same total PTO coefficient

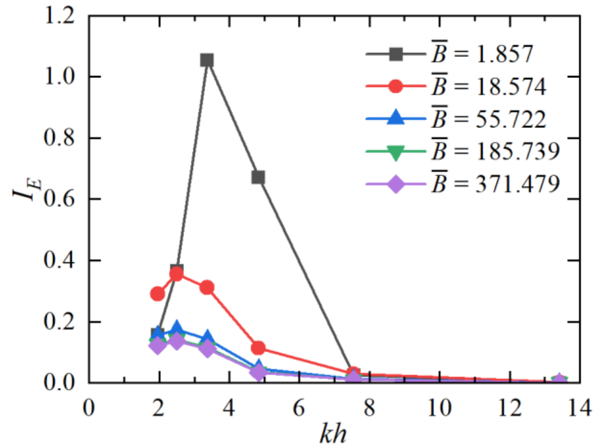

Fig. 24 The indicator I_E versus *kh* under different linear PTO coefficients

In Fig. 23, the linear PTO coefficient of the single-buoy WEC is three times as that of each buoy in the multi-buoy WEC. When $\bar{B}$ is less than 371.479, the absorbed power of the single-buoy WEC is less than that of the multi-buoy WEC; with the increase of the linear coefficient, the difference in power between those two WECs gradually shrinks. This rule can be easily captured by I_E shown in Fig. 24. Fig. 24 also shows that, compared to the sing-buoy WEC, the most significant improvement in power performance of the multi-buoy WEC is obtained at kh = 3.37 and $\bar{B}$ = 1.857 where the absorbed power is doubled. With the increase of PTO force, I_E gradually decreases to nearly zero but it is unlikely to be negative since when $\bar{B}$ is more than 371.479 both the single-buoy and multi-buoy WEC don’t capture wave energy as shown in Figs. 20 and 21. In general, the multi-buoy WEC is more suitable to be chosen in the current wave condition and PTO system.

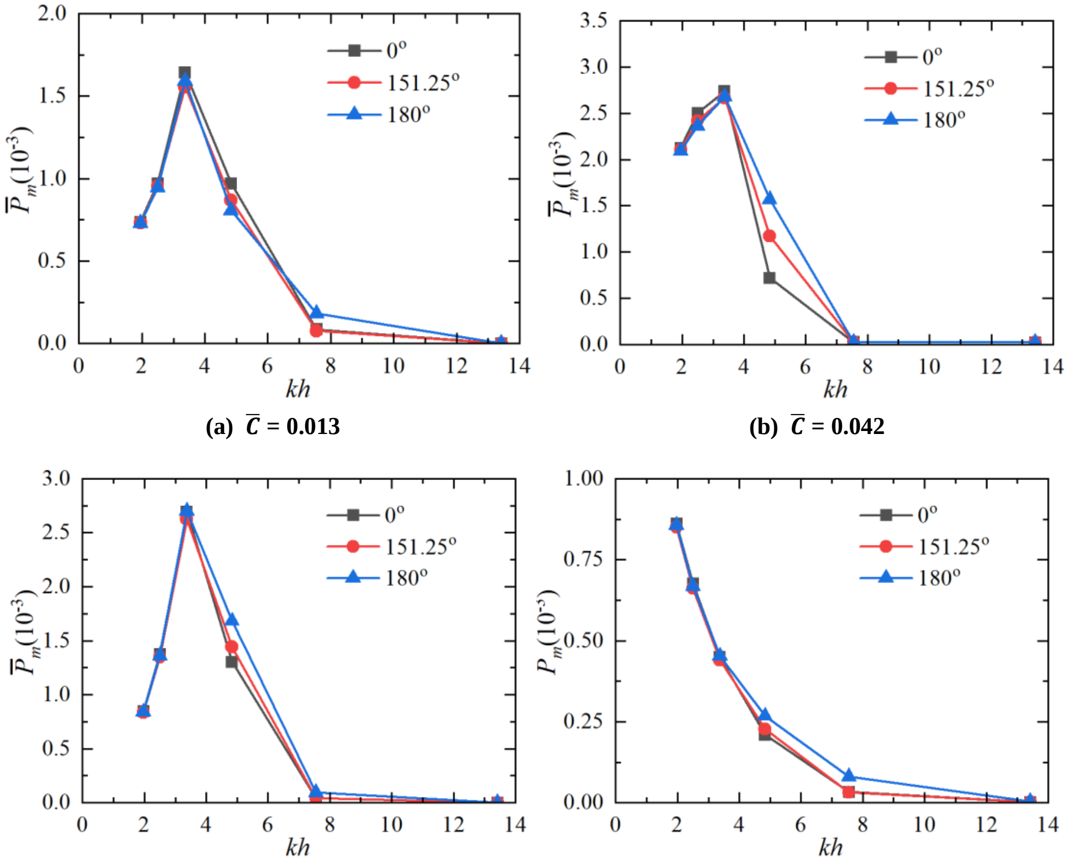

(a) $\overline{C}$ = 0.013 (b) $\overline{C}$ = 0.042

(c) $\overline{B}$ = 0.619 (b) $\overline{B}$ = 18.574

Fig. 25 Absorbed power of multi-buoy versus wave frequency *kh* with wave direction of 0, 151.25 and 180 degrees and different PTO forces

Unlike the single-buoy system, the multi-buoy system is not isotropous as the preliminary investigation shown in Section 4.1. The wave directionality may influence the power performance of the WEC. To shed some light on this, different wave directionalities are utilized in the investigations. Fig. 25 compares the power performance of the multi-buoy WEC in the cases with different incident wave angles, i.e. 0°, 151.25° and 180°. Both the linear and coulomb PTO models are considered. It is observed that the power performance of the multi-buoy WEC seems to be less sensitive to the wave directionality in most of the cases. However, when the PTO constant $\overline{C}$ = 0.042 (Fig. 25(b)), the absorbed power of the multi-buoy WEC is significantly higher when the incident wave angle is 180°, compared to the cases with the incident wave angle of 0°. This feature is useful in practices because the wave may come from any directions in reality. By choosing appropriate PTO model, the multi-buoy WEC does not consider to control the heading of the device to secure a satisfactory power production.

5. Conclusion

In this study, a novel hybrid system, which integrates a multi-buoy WEC with the IEA 15 MW wind turbine in a fixed monopile foundation, is proposed. The site condition is featured from the sea area around Shandong, China. The concept is developed from an existing concept which combines a torus shape heaving buoy with a fixed monopile foundation. The novelty of breaking down the torus buoy into three identical buoys is established based on the hypothesis that each buoy is subjected to less damping and thus has a more significant motion response compared with the corresponding torus WEC. As the dimension of the OWT and the WEC increases following the up-scaling trend of the OWT development, the wavelength become relatively shorter and smaller dimension of each buoy of the multi-buoy WEC may perform better. To confirm this, three-dimensional numerical models are established in ANSYS-Aqwa. In this proof-of-concept investigation, only the operational wave conditions without accompanied current are considered.

Since the multiple buoys are installed surrounding the monopile foundation in close proximity, the hydrodynamic interaction and the coupling effects become important, as confirmed by the hydrodynamic investigations on the motion responses and the force on a specific buoy with or without accompanied by other buoys. Different wave directionalities and PTO arrangements are considered in the investigation. On this basis, the systematic investigation of the power performance of the multi-buoy WEC integrated with the fixed monopile foundation is carried out. The results are compared with the corresponding results from the single-buoy WEC, which is a torus buoy with the equivalent geometry, motion properties and PTO damping to the multi-buoy WEC. Two types of PTO models are used. When the Coulomb PTO is applied, the power performance of the multi-buoy WEC is better than the single-buoy WEC in the cases where WECs can capture wave energy; for specific PTO, the peak value of the absorbed power from the multi-buoy WEC occurs at a higher frequency, compared with the single-buoy WEC, implying that the multi-buoy WEC is more suitable for absorbing power at smaller wave periods (higher *kh*). If the linear PTO model is applied, the superiority of the multi-buoy WEC is also observed at a specific range of the PTO coefficients. The numerical investigation also concluded that the power performance of the present system seems to be not sensitive to the wave directionality if an appropriate PTO model is applied.

Despite of the promising features of the proposed hybrid system discussed above, a few further comments may be added to inspire future research. The first one is the limitation of the linear potential theory used in this work. Based on the analysis of the Re and KC numbers, the problem described in this work is in the diffraction field and the viscous effect may be insignificant overall. This drives the use the potential theory, as many other existing research. However, when the wave frequency is close to the natural frequency of the WECs, and/or gap resonance occurs, the linear potential theory may over-predict the motion response and thus the power performance. This can be overcome by introducing calibrated artificial viscosity in the present model with the aid of the experimental or CFD work in the future. However, existing literature also conclude that such viscous effect may be linear and does not affect the qualitative conclusion [34]. The second issue is that identical PTO models are applied to all buoys in the multi-buoy WEC, for simplicity of the numerical work. In practice, the PTO systems needs to be optimised and different PTO coefficients may be applied to different buoys subjected to an instantaneous wave condition. A multi-function optimisation and control strategy may be tested in the near future. Finally, the power generated by the WEC is at the level of hundreds kW, which seems to be minuscule compared with the wind power generation. However, one may admit that by sharing the foundation with the OWT, the cost of the wave energy would be reduced and the integrated WEC may reduce the wave load on the OWT, reducing the fatigue of the OWT, whereas it does not affect the power production of the wind turbine since the foundation is fixed.

Acknowledgment

The authors acknowledge the support from Shandong Provincial Natural Science Foundation (Grant No. ZR2021ZD23), National Natural Science Foundation of China (Grant No. 52271297), National Natural Science Foundation of China (Grant No. 52071303), Shandong Provincial Natural Science Foundation (Grant No. ZR2022ME002), National Natural Science Foundation of China (Grant No. U22A20216), Taishan Scholars Program of Shandong Province (No. ts20190914) and Chinese Scholarship Council (CSC, China).

Reference

[1] Y. Li, S. Liu, C. Xu, D. Li, H. Shi, Experimental study on the cylindrical oscillating water column device, Ocean Eng. 246 (2022). https://doi.org/10.1016/j.oceaneng.2022.110523.

[2] S. Astariz, G. Iglesias, Selecting optimum locations for co-located wave and wind energy farms. Part II: A case study, Energy Convers. Manag. 122 (2016) 599–608. https://doi.org/10.1016/j.enconman.2016.05.078.

[3] M.F. Howland, S.K. Lele, J.O. Dabiri, Wind farm power optimization through wake steering, Proc. Natl. Acad. Sci. U. S. A. 116 (2019) 14495–14500. https://doi.org/10.1073/pnas.1903680116.

[4] T. Sun, Z. Zhang, Optimal control and performance evaluation of an inerter-based point absorber wave energy converter, Ocean Eng. 259 (2022). https://doi.org/10.1016/j.oceaneng.2022.111883.

[5] L. Cradden, C. Kalogeri, I.M. Barrios, G. Galanis, D. Ingram, G. Kallos, Multi-criteria site selection for offshore renewable energy platforms, Renew. Energy. 87 (2016) 791–806. https://doi.org/10.1016/j.renene.2015.10.035.

[6] M. Chen, R. Wang, P. Xiao,l. Zhu, Numerical analysis of a floating semi-submersible wind turbine integrated with a point absorber wave energy convertor//The 30th International Ocean and Polar Engineering Conference. OnePetro, 2020.

[7] Y. Wang, L. Zhang, C. Michailides, L. Wan, W. Shi, Hydrodynamic response of a combined wind-wave marine energy structure, J. Mar. Sci. Eng. 8 (2020). https://doi.org/10.3390/JMSE8040253.

[8] Y. Wang, W. Shi, C. Michailides, L. Wan, H. Kim, X. Li, WEC shape effect on the motion response and power performance of a combined wind-wave energy converter, Ocean Eng. 250 (2022). https://doi.org/10.1016/j.oceaneng.2022.111038.

[9] Y. Li, M.C. Ong, K. Wang, L. Li, Z. Cheng, Power performance and dynamic responses of an integrated system with a semi-submersible wind turbine and four torus-shaped wave energy converters, Ocean Eng. 259 (2022). https://doi.org/10.1016/j.oceaneng.2022.111810.

[10] H. Lee, S.K. Poguluri, Y.H. Bae, Performance analysis of multiple wave energy converters placed on a floating platform in the frequency domain, Energies. 11 (2018). https://doi.org/10.3390/en11020406.

[11] J. Hu, B. Zhou, C. Vogel, P. Liu, R. Willden, K. Sun, J. Zang, J. Geng, P. Jin, L. Cui, B. Jiang, M. Collu, Optimal design and performance analysis of a hybrid system combing a floating wind platform and wave energy converters, Appl. Energy. 269 (2020). https://doi.org/10.1016/j.apenergy.2020.114998.

[12] Y. Si, Z. Chen, W. Zeng, J. Sun, D. Zhang, X. Ma, P. Qian, The influence of power-take-off control on the dynamic response and power output of combined semi-submersible floating wind turbine and point-absorber wave energy converters, Ocean Eng. 227 (2021). https://doi.org/10.1016/j.oceaneng.2021.108835.

[13] M. Kamarlouei, J.F. Gaspar, M. Calvario, T.S. Hallak, M.J.G.C. Mendes, F. Thiebaut, C. Guedes Soares, Experimental study of wave energy converter arrays adapted to a semi-submersible wind platform, Renew. Energy. 188 (2022) 145–163. https://doi.org/10.1016/j.renene.2022.02.014.

[14] M.J. Muliawan, M. Karimirad, T. Moan, Dynamic response and power performance of a combined Spar-type floating wind turbine and coaxial floating wave energy converter, Renew. Energy. 50 (2013) 47–57. https://doi.org/10.1016/j.renene.2012.05.025.

[15] M.J. Muliawan, M. Karimirad, Z. Gao, T. Moan, Extreme responses of a combined spar-type floating wind turbine and floating wave energy converter (STC) system with survival modes, Ocean Eng. 65 (2013) 71–82. https://doi.org/10.1016/j.oceaneng.2013.03.002.

[16] N. Ren, Z. Gao, T. Moan, L. Wan, Long-term performance estimation of the Spar-Torus-Combination (STC) system with different survival modes, Ocean Eng. 108 (2015) 716–728. https://doi.org/10.1016/j.oceaneng.2015.08.013.

[17] L. Wan, Z. Gao, T. Moan, Model Test of the STC Concept in Survival Modes, (2014). https://doi.org/10.1115/OMAE2014-23213.

[18] L. Wan, Z. Gao, T. Moan, Experimental and numerical study of hydrodynamic responses of a combined wind and wave energy converter concept in survival modes, Coast. Eng. 104 (2015) 151–169. https://doi.org/10.1016/j.coastaleng.2015.07.001.

[19] L. Wan, Z. Gao, T. Moan, C. Lugni, Experimental and numerical comparisons of hydrodynamic responses for a combined wind and wave energy converter concept under operational conditions, Renew. Energy. 93 (2016) 87–100. https://doi.org/10.1016/j.renene.2016.01.087.

[20] L. Wan, M. Greco, C. Lugni, Z. Gao, T. Moan, A combined wind and wave energy-converter concept in survival mode: Numerical and experimental study in regular waves with a focus on water entry and exit, Appl. Ocean Res. 63 (2017) 200–216. https://doi.org/10.1016/j.apor.2017.01.013.

[21] C. Zhao, P.R. Thies, Q. Ye, J. Lars, System integration and coupled effects of an OWT/WEC device, Ocean Eng. 220 (2021). https://doi.org/10.1016/j.oceaneng.2020.108405.

[22] N. Ren, Z. Ma, B. Shan, D. Ning, J. Ou, Experimental and numerical study of dynamic responses of a new combined TLP type floating wind turbine and a wave energy converter under operational conditions, Renew. Energy. 151 (2020) 966–974. https://doi.org/10.1016/j.renene.2019.11.095.

[23] J. S. Rony, D. Karmakar, Coupled dynamic analysis of hybrid offshore wind turbine and wave energy converter. J. Offshore Mech. Arct. Eng., 144(2022). https://doi.org/10.1115/1.4052936.

[24] Li, Y., Yan, S., Shi, H., Ma, Q., Dong, X., Cao, F., 2023. Wave Load Characteristics on a Hybrid Wind-Wave Energy System. Ocean Eng. (under review)

[25] L. Arany, S. Bhattacharya, Simplified load estimation and sizing of suction anchors for spar buoy type floating offshore wind turbines, Ocean Eng. 159 (2018) 348–357. https://doi.org/10.1016/j.oceaneng.2018.04.013.

[26] N. Ren, Z. Ma, T. Fan, G. Zhai, J. Ou, Experimental and numerical study of hydrodynamic responses of a new combined monopile wind turbine and a heave-type wave energy converter under typical operational conditions, Ocean Eng. 159 (2018) 1–8. https://doi.org/10.1016/j.oceaneng.2018.03.090.

[27] E. Homayoun, H. Ghassemi, H. Ghafari, Power performance of the combined monopile wind turbine and floating buoy with heave-type wave energy converter, Polish Marit. Res. 26 (2019) 107–114. https://doi.org/10.2478/pomr-2019-0051.

[28] M.J. Khatibani, M.J. Ketabdari, Numerical modeling of an innovative hybrid wind turbine and WEC systems performance: A case study in the Persian Gulf, J. Ocean Eng. Sci. (2022). https://doi.org/10.1016/j.joes.2022.05.008.

[29] S. Gkaraklova, P. Chotzoglou, E. Loukogeorgaki, Marine Science and Engineering Frequency-Based Performance Analysis of an Array of Wave Energy Converters around a Hybrid Wind-Wave Monopile Support Structure, (2020). https://doi.org/10.3390/jmse.

[30] C. Perez-Collazo, R. Pemberton, D. Greaves, G. Iglesias, Monopile-mounted wave energy converter for a hybrid wind-wave system, Energy Convers. Manag. 199 (2019). https://doi.org/10.1016/j.enconman.2019.111971.

[31] Y. Zhou, D. Ning, W. Shi, L. Johanning, D. Liang, Hydrodynamic investigation on an OWC wave energy converter integrated into an offshore wind turbine monopile, Coast. Eng. 162 (2020). https://doi.org/10.1016/j.coastaleng.2020.103731.

[32] P. Cong, B. Teng, W. Bai, D. Ning, Y. Liu, Wave power absorption by an oscillating water column (OWC) device of annular cross-section in a combined wind-wave energy system, Appl. Ocean Res. 107 (2021). https://doi.org/10.1016/j.apor.2020.102499.

[33] M. Kamarlouei, J.F. Gaspar, M. Calvario, T.S. Hallak, M.J.G.C. Mendes, F. Thiebaut, C. Guedes Soares, Experimental analysis of wave energy converters concentrically attached on a floating offshore platform, Renew. Energy. 152 (2020) 1171–1185. https://doi.org/10.1016/j.renene.2020.01.078.

[34] I. Ekerhovd, M. Chen, P.H. Taylor, W. Zhao, Numerical study on gap resonance coupled to vessel motions relevant to side-by-side offloading, Ocean Eng. 241 (2021) 110045. https://doi.org/10.1016/j.oceaneng.2021.110045.

[35] E. Gaertner, J. Rinker, L. Sethuraman, F. Zahle, B. Anderson, G. Barter, N. Abbas, F. Meng, P. Bortolotti, W. Skrzypinski, G. Scott, R. Feil, H. Bredmose, K. Dykes, M. Shields, C. Allen, A. Viselli, IEA Wind - Offshore Reference Wind - 15MW, (2020).
[36] H.R. Ghafari, H. Ghassemi, A. Neisi, Power matrix and dynamic response of the hybrid Wavestar-DeepCwind platform under different diameters and regular wave conditions, Ocean Eng. 247 (2022). https://doi.org/10.1016/j.oceaneng.2022.110734.
[37] X. chen Dong, Z. Gao, D. min Li, S. ting Huang, H. da Shi, Power Absorption of A Two-Body Heaving Wave Energy Converter Considering Different Control and Power Take-off Systems, China Ocean Eng. 36 (2022) 15–27. https://doi.org/10.1007/s13344-022-0001-3.